RSC Advances

ROYAL SOCIETY OF CHEMISTRY

www.rsc.org/advances

Enhanced polarization of hydroxyapatite using the design concept of functionally graded materials with sodium potassium niobate

A. K. Dubey[1,*], K. Kakimoto[1], A. Obata[2] and T. Kasuga[2]

[1]Department of Materials Science and Engineering, [2]Department of Frontier Materials, Graduate School of Engineering, Nagoya Institute of Technology, Gokiso-cho, Showa-ku, Nagoya 466-8555, Japan.

Abstract

The present work aims to enhance the electrical activities of hydroxyapatite (HA) without affecting its' bioactivity through the development of functionally graded materials (FGM) using biocompatible sodium potassium niobate (NKN) piezoelectrics as an intermediary layer. The NKN layer was sandwiched between HA layers via buffer interlayers (abbreviated as HA-NKN-HA) and optimally processed using spark plasma sintering route. The dielectric and electrical properties were studied over a wide range of temperatures (25-500 ^{0}C) and frequencies (10^{-1}-10^6 Hz). *In vitro* cellular response in terms of initial cell adhesion and proliferation on the FGM as well as corresponding monoliths was assessed using human osteoblast-like SaOS2 cells. The reasonably good combination of dielectric and electrical properties, such as dielectric constant (38), AC conductivity [5.5×10^{-9} (ohm-cm)$^{-1}$], piezoelectric strain coefficient (4.2 pC/N), electromechanical coupling coefficient (0.17), mechanical quality factor (81) and remnant polarization (0.06 μC/cm^2) in reference to the natural bone has been achieved with the developed FGM. The mechanism of conduction remains similar in FGM as that of pure HA. Impedance analyses suggest the occurrence of two polarization processes in HA and NKN monoliths, whereas more than two polarization processes are observed in the FGM. The significant increase in cell proliferation with culture duration of up to 5 days suggests that developed FGM favors the cell growth and proliferation. In addition, the present study also establishes the superior

cytocompatibility of the perovskite NKN phase. The developed FGM can be a potential substitute for electro-active orthopedic prosthetic implant applications.

Keywords: Hydroxyapatite, Sodium potassium niobate, Piezo-biomaterial, Electrical activity, *In vitro*.

*Correspondence: akdbhu@gmail.com (A.K. Dubey) Tel. & Fax: +81 52 735 7734

1. Introduction

The bioelectricity in the living bone has been recognized in terms of piezoelectricity, pyroelectricity, streaming potential, ferroelectricity etc., which directs the various bone metabolic activities.[1-5] For example, piezoelectricity has an important role in controlling bone growth and structure as well as repairing the bone fractures.[6-9] Because of these electromechanical couplings, the bone acts like transducer.[10] Mascarenhas suggested the bone as a 'bioelectret'.[11] The living bone is also characterized as a functionally graded material and this gradation facilitates the bone to perform its biophysical and biochemical activities.[12-14] In addition to the inherent electrical properties of bone, the polarization of implants or the application of external electrical stimulation has been suggested to enhance the bone growth as well as bone fracture healing.[15-19] The potentiality of these electrical stimuli in enhancing the growth and proliferation of fibroblast as well as osteoblast cells has been demonstrated by a number of studies.[20-23] Therefore, the development of electrically active prosthetic implant can provide better functional response in terms of effective osseointegration and relatively longer survival period.

Because of excellent bioactivity and structural correspondence with the mineral component of living bone, hydroxyapatite (HA) has been found as one of the most pledging orthopedic material.[24,25] However, the widespread use of HA is restricted by it's brittle nature and poor electrical properties. To this backdrop, the piezoelectric biocompatible material can be an interesting choice. The sodium potassium niobate (NKN) possesses reasonably high values of electromechanical coupling coefficient (0.44), mechanical quality factor (280), piezoelectric strain coefficient (d_{33}, 161 pC/N) and dielectric constant (657).[26] The ferroelectric NKN ($Na_xK_yNbO_3$; $0 \leq x \leq 0.8$ and $0.2 \leq y \leq 1$) has been patented as a potential biocompatible material by evaluating the lactate dehydrogenase (LDH) activity of human monocytes.[27] The advantage of

directional and spatial polarization of such ferroelectric material in terms of the tissue growth and regeneration has also been discussed.[27] The niobate ceramics has been suggested as a promising substitute for bone tissue applications.[28,29] Navarrete et al.[30] demonstrated the better cellular response of Nb coatings on stainless steel substrates as compared to uncoated steel in terms of initial adhesion and proliferation of human osteoblast cells.

As the polarization processes have been suggested to play a key role in the normal bone functioning, the present work aims to increase the polarizability of HA without affecting its' bioactivity by developing the functionally graded material (FGM) with piezoelectric sodium potassium niobate [$(Na_{0.5}K_{0.5})NbO_3$, NKN] ceramic. Because of the difference in the coefficients of thermal expansions between HA ($14x10^{-6}/^0C$)[31] and NKN ($8x10^{-6}/^0C$)[32] phases, a buffer layer containing HA and NKN in molar ratio of 1:7 (optimized) has been introduced between HA and NKN layers to avoid the peeling off or crack formation between the layers due to the thermal mismatch and then sintered using spark plasma sintering (SPS) route. Further, the detailed dielectric and electrical properties of the developed FGM has been studied in reference to it's corresponding constituent phases as well as living bone. In addition, the initial adhesion and proliferation behavior of human osteoblast-like SaOS2 cells on the developed samples have also been examined.

2. Experimental

2.1 Materials Processing

The HA nanopowders were obtained from Sigma Aldrich, USA. The NKN was synthesized in-house by solid state ceramic route using stoichiometric amounts of high purity (99.99%) Na_2CO_3, Nb_2O_5 and K_2CO_3 powders as starting materials.[33] The mixed powders were ball milled for 24 hrs using polyethylene jar and zirconia balls (Φ 5 mm) with the acetone as milling

medium. Following this, the slurry was dried using rotary vacuum evaporator (Eyela, N-1100) and oven. The dried powders were then calcined at 910^{o}C for 10 hrs. The X-ray diffraction (XRD, Cu-Kα; Philips X'pert, MPD) analysis confirmed the formation of single phase NKN.

The spatial distribution of different layers in the developed FGM and their corresponding thicknesses is shown in Fig. 1 (a). The layers were stacked in order of HA - buffer - NKN - buffer - HA (abbreviated as HA-NKN-HA). The thicknesses of the HA, buffer and NKN layers are 0.2, 0.15 and 0.5 mm, respectively. The layered green compacts were pre-pressed at 40 MPa and then consolidated using spark plasma sintering (SPS) route at 980^{0}C for 10 min with heating rate of 50^{0}C/min, followed by furnace cooling [Fig. 1 (b)]. A pressure of 50 MPa was applied during the final stage of consolidation. For comparing the results, pure HA and NKN composites were also sintered using similar processing conditions with the pressure of 80 MPa. In order to remove the carbon contamination, the SPSed samples were annealed in air at 700^{0}C for 2 hrs. It has been reported that the reduced atmosphere sintering of NKN can restrain the volatilization of alkali elements (Na and K) as well as provides better densification, which is rather difficult using conventional sintering in air.[34] In addition, the spark plasma sintering of NKN ceramic system can provide the better functional (dielectric, piezoelectric and ferroelectric) properties as compared to those of the conventionally sintered samples.[35] Therefore, the spark plasma sintering was performed to obtain dense and stoichiometric NKN phase.

2.2 Phase evaluation and morphological characterization

The sintered samples with diameter and thickness of 15 and 1.2 mm, respectively, were polished. The XRD analysis was performed to verify the phases present in the SPSed compacts. The fractured surfaces of the developed FGM were characterized by scanning electron microscopy (SEM, Jeol JSM-7001F).

2.3 Dielectric and electrical characterization

For dielectric and electrical measurements, the mirror polished samples were electroded with Ag-Pd paste and cured at 700^0C for 5 min. The dielectric response of the samples was recorded using impedance analyzer (Agilent 4292A) over a wide range of temperature (25-500^0C) and frequency (40 Hz - 1 MHz). The samples were heated at a heating rate of 3^0C/min. The data was collected during the cooling cycle and the dielectric constant ($\varepsilon_r = C.d/\varepsilon_0 A$; where, C, d and A are capacitance, thickness and area of the samples, respectively and ε_0 is the permittivity of free space) and alternating current (AC) conductivity [$\sigma_{ac} = G.d/A$; where, conductance $G = \omega C.D$; ω $(= 2\pi f)$ and D are the angular frequency and dielectric loss, respectively] were calculated. The low frequency (up to 10^{-1} Hz) dielectric and electrical responses of the samples were measured upto to 500^0C using LCR meter (NF ZM2355). From the obtained impedance data, a wide spectra of dielectric constant [$\varepsilon_r = -Z^{//}.t/(Z^{/2} + Z^{//2}).\varepsilon_0\omega A$; where, $Z^{/}$ and $Z^{//}$ represent the real and imaginary parts of the impedance], AC conductivity [$\sigma_{ac} = Z^{/}.t/(Z^{/2} + Z^{//2})\ A$] and phase angle [$\theta = \tan^{-1}(Z^{//}/Z^{/})$] with frequency and temperature were studied.[36] The value of piezoelectric strain coefficient (d_{33}) was measured using d_{33} meter (ZJ-6B). The ferroelectric response of the poled samples was evaluated by Ferroelectric Tester (TF2000FE-HV aixACT) at 1 Hz of frequency. The electrical poling (E = 2 kV/mm) of the samples was performed at 150^0C for 30 min in silicon oil. The samples were then cooled down with the continuous exposure of electric field.

The electromechanical coupling coefficient (K_p) and mechanical quality factor (Q_m) were calculated by resonance-antiresonance method based on IEEE standards.

2.4 *In vitro* cytocompatibility evaluation

2.4.1 Cell culture experiments

In order to evaluate the cellular response in terms of initial cell adhesion, morphological as well as proliferation behavior, human osteoblast-like SaOS2 (ECACC, UK) cells were cultured on the developed FGM as well as it's corresponding monoliths. The growth media for SaOS2 cells contain McCoy's 5A medium (Gibco, USA) supplemented with 10% Fetal bovine serum (FBS, Gibco) and 1% antibiotics (Pen Strep, Gibco). Before seeding the cells, the samples were sterilized by soaking in 70% ethanol and UV exposure for 30 min. The density of SaOS2 cells were evaluated using hemocytometer. The cells with the densities of $2.5x10^4$ SaOS2 cells/well in 48 well plate were seeded on the samples and incubated (5% CO_2, 95% relative humidity) for 30 min at 37^0C. After 30 min of incubation, the respective growth media (0.5 ml/ well) were added and incubated further for the desired period of time (up to 5 days). The culture media was changed at every alternate day. The repeatability of results was verified by three independent set of culture experiments and the triplicates of the samples with the surface area of 0.44 cm^2 were used in each case.

2.4.2 Morphological observations

The initial adhesion and morphology of cells were examined after 6 hrs of culture. The adhered cells were fixed in 4% paraformaldehyde phosphate buffer for 30 min at 4^0C. Subsequently, the cells were permeabilized with 0.1% Triton X-100 (diluted in PBS) and 1% bovine serum albumin for 25 min at 4^0C. Following this, the actin filaments of the cells were stained using 2.5 % (in PBS) Alexa Fluor 488 Phalloidin (Molecular Probes, USA) fluorescent dye for 30 min at 37^0C. The DAPI (VECTASHIELD Mounting Medium with DAPI, Vector Laboratories, USA)

was used to stain the nuclei of cells. The morphological observations were performed using fluorescence microscope (BIOREVO BZ9000, Keyence, Japan).

2.4.3 Proliferation assay

The cell proliferation was evaluated after 1, 3 and 5 days of culture on the samples, respectively. After the respective culture durations, the cells were incubated with the reagent of the cell counting kit-8 (CCK-8, Dojindo, Japan) for 2 hrs at 37^0C following the manufacturer 's protocol. The number of the cells were calculated by quantifying the medium absorbance at a wavelength of 450 nm with the microplate reader (Sunrise Remote, Tecan, Switzerland) using CCK-8.

2.4.4 Statistical analysis

The statistical analysis was performed with SPSS-13 (statistical package for social sciences, IBM) software. The ANOVA method was used to evaluate the significant difference in cell proliferation as a function of culture duration. The Post Hoc multiple comparisons were carried out using Tukey and Games-Howell tests at $p < 0.05$.

3. Results and Discussion

3.1 Phase identification and microstructural characterization

Fig. 2 shows the XRD patterns of the HA and NKN monoliths as well as functionally graded HA-NKN-HA sample. The processing condition was optimized to achieve the maximum density and single phase perovskite NKN, which is quite difficult using conventional solid state sintering route because of the volatization of alkali elements. The XRD data are indexed in reference to the orthorhombic phase of the perovskite NKN and hexagonal HA. Using the above processing condition, the single phase HA and NKN with the densities of about 99% of their respective theoretical values are obtained. The density of HA-NKN-HA samples was 3.93 gm/cm^3.

Fig. 3 demonstrates the SEM images of the fractured surfaces, captured around the interfacial regions between HA and buffer [Figs. 3 (a) and (c)] as well as buffer and NKN [Figs. 3 (b) and (d)] layers. The transgranular mode of fracture occurs at the HA and buffer interface. However, the transgranular as well as intergranular fractures can be seen at the NKN and buffer interface. A very small fraction of residual porosity has been observed in the interfacial regions. The cracks due to the delamination of layers were not observed at any of the interfaces. However, the finer scale polishing revealed insignificant cracks at HA surface, probably because of the very small particle size of the HA (< 200 nm) than that of the NKN phase (~ μm). As compared with the initial particle sizes, more grain growth has been observed for HA as compared to the NKN phase. The absence of the cracks at the interfacial regions suggest that the inserted buffer layer significantly reduced the thermal stresses between HA and NKN phases, despite of very fast SPS cooling rates (~ 250^0C/min).

3.2 Dielectric behavior

Figs. 4 (a), (c) and (e) demonstrate the variation of dielectric constant and loss with temperature at frequencies of 1, 10 and 100 kHz. The dielectric behavior with temperature for pure HA is almost similar to that reported by Orlovskii et al.[37] The increase in the dielectric constant with temperature is accompanied by the respective peaks in the dielectric loss curve due to the relaxation of space charge and dipolar polarizations.[37] With the increase in frequency from 1 to 100 kHz, the relaxation peaks reallocated themselves in the higher temperature regions satisfying the relationship, $\omega\tau = 1$. In case of pure NKN [Fig. 4 (c)], the dielectric anomalies at about 200^0C signify the characteristic transition from orthorhombic to tetragonal (T_{ot}) phase. The dielectric loss curves reveal peaks at temperature of 188^0C, where the sharp increase in the dielectric constant curve is observed. This phenomenon is probably associated with the relaxation of space charge polarization. The T_{max} corresponding to the Curie temperature of NKN was observed at

410^0C (not shown). The dielectric behavior of HA-NKN-HA sample [Fig. 4 (e)] follows the similar trend with temperature and frequency as that of pure HA [Fig. 4 (a)]. The sharp increase in the dielectric loss in HA-NKN-HA sample at temperature above 200^0C is attributed to the space charge polarization, which arises due to the presence of various layers with different electrical conductivities as well as microstructural features. The room temperature dielectric constant values for HA, NKN and HA-NKN-HA samples at a frequency of 10 kHz are 12, 610 and 39, respectively. It is, therefore, clear that the polarization of hydroxyapatite has increased more than three times with the concept of functionally graded material using NKN as an intermediary layer.

Figs. 4 (b), (d) and (f) demonstrate the variation of dielectric constant with frequency at a few isothermal temperatures. The dielectric constant decreases with increase in frequency and this dielectric dispersion with frequency is more significant at higher temperatures (> 200^0C) and lower frequencies (< 100 Hz) representing the relaxation of interfacial or space charge polarization. However, in case of HA-NKN-HA, prominent dispersion is observed at all measuring frequencies because of the presence of additional relaxation phenomenon associated with the multi-layered configuration. The dielectric constant is higher at frequencies less than 1 kHz due to the contribution of the various polarization processes (space charge and dipolar). Also, the dispersion in the dielectric constant in the low frequency (<1 kHz) and high temperature (> 100^0C) range is indicative of the presence of dc conductivity in the developed samples.[38,39] At very low frequencies ($f << 1/2\pi RC$), the overall electrical response of the materials is decided by the resisters as the capacitors turn out to be an open circuit.[40] The polarization processes get terminated successively with increase in frequency, which initiates with space charge (Maxwell-Wagner) polarization and offer the intrinsic dielectric constant

values for the sample. At high frequencies (> 50 kHz), all the samples appear to attain a constant value with further increase of frequency due to the relaxation of the involved polarization processes in the measured frequency range. The presence of conductivity, due to the spark plasma sintering in vacuum, has a major role in the observed dielectric dispersion. The similar dielectric dispersion behavior is reported for the bone tissue as well.[41] Depending upon the frequency, the α (< 10 kHz), β (~ MHz) and γ (~ GHz) dispersions has been suggested in the biological tissues, which is associated with the various polarization processes.[42,43] In the dried human cortical bone sample, the dielectric relaxation has been obtained at about 85^0C and suggested to be associated with the dipolar polarization.[44] Because of the ferroelectric nature, the bone possesses spontaneous polarization, i.e., permanent electric dipole moment. The dielectric constant of bone is reported to be about 10.[45] Williams and Saha suggested that the dielectric and electrical properties of bone can be speculated from it's density, where the specific capacitance depend strongly on the bone density.[46] The frequency and temperature dependent dielectric response of the developed samples can be explained on the basis of the following mechanisms:

The HA is an ionic crystal, where the polarization mechanism is dominated by the response of hydroxyl (OH^-) ions.[20,47] In HA, the OH^- ions are positioned at the centre of the equilateral triangle formed by Ca^{2+} ions and the dipoles due to OH^- ions are aligned vertically to the base of the triangles.[47-49] The orientation of OH^- dipoles has an important role in the dielectric and electrical behaviors of HA at a given temperature and frequency.[50] The temperature induced orientation of OH^- dipoles has been suggested as one of the key factors responsible for the phase transition of HA.[49,50] The low temperature (< 150^0C) dielectric behavior of HA is associated with the processing related structural defects, O_2 molecules as well as O^- and OH^- ions. [49,51] In addition to the space charge polarization, the rapid increase in dielectric constant with temperature is

probably associated with the alignment of polar OH groups[52] which was then followed by the phase transformation from monoclinic (belongs to crystallographic space group: $P2_1/b$) to hexagonal ($P6_3/m$) phase at temperature of about 200^0C. [49,50] In addition to the alignment of OH^- ions, their displacement also contribute to HA polarization.[53] Horiuchi et al.[50] suggested the existence of persistent polarization in HA due to the crystal OH^- defect. At elevated temperatures (> 300^0C), the dielectric behaviors of HA an NKN are governed by the thermally activated polarization via thermal energy induced defects and their movement.[54]

3.3 AC Conductivity behavior

Figs. 5(a), (b) and (c) demonstrate the variation of AC conductivity with temperature at frequencies of 1, 10 and 100 kHz for HA, NKN and HA-NKN-HA samples. In case of pure HA and HA-NKN-HA, the conductivity increases with temperature in exponential manner and after attaining the maxima, it is found to vary linearly with further increase in temperature. The maxima represent the relaxation process. The position of the peaks shifted to the higher temperature region with increase of frequency from 1 to 100 kHz. The conductivity of each peak maximum is plotted with the respective temperature, as shown in Fig. 5 (d). The linear variation of conductivity with temperature suggests to follow the Arrhenius relationship, $\sigma = \sigma_0 \exp(-E_a/kT)$, where σ_0, E_a and k are the pre-exponential factor, activation energy and Boltzmann constant, respectively. The values of activation energies for HA and HA-NKN-HA was calculated to be 0.78 and 0.69 eV, respectively. This activation energy is suggested to be associated with the proton conduction in HA. [53,55] It can therefore be inferred that the mechanism of conduction remains similar after incorporation of NKN layer. The variation in AC conductivity with temperature for graded HA-NKN-HA sample is found to follow the similar trend as that of pure HA. In case of pure NKN, the characteristic phase transitions, from

orthorhombic to tetragonal (ferroelectric) and tetragonal to cubic (paraelectric) phase, are clearly evident at about 200^0C and 400^0C, respectively. The variation of AC conductivity with frequency was observed to follow the Jonscher's power law expression,[56] $\sigma_{ac}\ \alpha\ (\omega)^n$, where ω is the angular frequency and exponent n is a constant, the value of which is depends upon the temperature and frequency (figure not shown). The room temperature AC conductivity values for HA, NKN and HA-NKN-HA samples at a frequency of 10 kHz are $1.5x10^{-9}$, $1.2x10^{-7}$ and $5.7x10^{-9}$ $(ohm\text{-}cm)^{-1}$, respectively. The AC conductivity of the natural bone has been reported to be of the order of 10^{-9}-10^{-10} $(ohm\text{-}cm)^{-1}$.[57] The room temperature DC resistivity (ρ_{dc}) values, obtained from the V-I relationship, for HA and HA-NKN-HA are $2.8x10^{14}$ and $2.0x10^{13}$ ohm-cm, respectively. The observed conductivity behavior for the developed compositions can be explained on the basis of the following mechanisms:

It has been reported that the high temperature sintering of HA results the formation of vacancies at hydroxyl (OH^-) sites in the crystal lattice.[58] The dehydration of lattice OH^- ions in HA is generally responsible for the observed conduction in HA.[59] Laghzizil et al.[60] suggested that the conduction of protons (H^+) among adjacent OH^- ions in HA describes the conduction mechanism according to the equation,

$$2\ OH^- + PO_4^{3-} \rightarrow O^{2-} + HPO_4^{2-} + OH \rightarrow O^{2-} + PO_4^{3-}\ HOH + \square_{OH^-} \quad (1)$$

Where, □ represents the vacancy.

The hopping of protons at the O^{2-} sites in HA can contribute to the increase in conductivity at higher temperatures, as can be realized from the equation, [59-61]

$$Ca_{10}\ (PO_4)_6(OH)_2 \rightarrow Ca_{10}\ (PO_4)_6\ (OH)_{2-2x}\ O_x\ \square_x + xH_2O \quad (2)$$

It has been demonstrated that the proton migration in the water, adsorbed on the surface of HA is one of the important factors responsible for the conduction in the lower temperature region (<

100^0C). [36-63] In case of NKN samples, reduced atmosphere sintering can restrain the volatility of alkali elements as per the expression,[34]

$$2(M)_M^* + \frac{1}{2}O_2 \leftrightarrow (M)_2O\ (gas) + 2\,V_M^{/} + 2h^{\bullet} \quad (3)$$

Where, M represents the alkali elements, Na and K. However, reduced atmosphere sintering led to the formation of oxygen vacancies,[34]

$$O_O^* \rightarrow \frac{1}{2}O_2 + V_O^{\bullet\bullet} + 2e^{/} \quad (4)$$

In the present case, the structural defects in HA due to dehydration associated to the spark plasma sintering appears to be responsible phenomenon for the observed conductivity behavior. In addition to the polar OH groups, the space charge is also playing an important role in increasing the AC conductivity with temperature.

3.4 Phase angle, piezoelectric and ferroelectric behavior

Figs. 6 (a), (b) and (c) demonstrate the variation of phase angle with frequency at a few selected temperatures. At a temperature of 500^0C, the phase angles for HA, HA-NKN-HA and NKN are close to 0^0 at lower frequencies (< 100 Hz), which indicates the presence of significant conductivity in these samples.[36] With increase in frequency, the phase angle decreases and approaches to approximately -90^0 at about 10 kHz of frequency (except HA-NKN-HA), which represents the capacitive response of the samples in the measured range of temperature and frequency.[36]

The piezoelectric strain coefficient (d_{33}) value, evaluated for the electrically poled HA-NKN-HA sample to be 4.2 pC/N. This suggests that the developed HA-NKN-HA functionally graded sample is piezoelectric in nature. As the natural bone is reported to act as a transducer, the measurement of electromechanical coupling coefficient (K_p) was also performed. For this calculation, the impedance and phase angle of the HA-NKN-HA sample has been recorded in the

frequency range of 110-130 kHz [Fig. 6(d)]. The value of K_p has been calculated to be 0.17. For the piezoelectric NKN, the value of K_p is reported to be about 0.4. The mechanical quality factor (Q_m) has been calculated by measuring the complex admittance in the similar frequency range as for K_p. The value of Q_m for HA-NKN-HA was found to be 81. Fig. 7 shows the P-E hysteresis behavior of the developed HA-NKN-HA sample. The presence of P-E hysteresis loop suggests that the developed HA-NKN-HA sample is ferroelectric in nature. The remnant polarization (P_r) and coercive field (E_c) values for HA-NKN-HA are 0.06 $\mu C/cm^2$ and 0.76 kV/cm, respectively. There are few studies demonstrated the ferroelectricity of the cortical bone.[5,64] For the dry cortical bone sample, the values of remnant polarization (P_r) and coercive field (E_c) are estimated to be about 0.60 nC/cm^2 and 0.70 kV/cm, respectively.[64]

3.5 Impedance spectroscopic analysis

Fig. 8 illustrates the complex plane impedance plots for HA, NKN and HA-NKN-HA samples at temperatures of 500^0C and 400^0C, respectively. The impedance analysis has been performed to reveal the grain and grain boundary contributions individually from the entire spectrum, in terms of their resistances and capacitances. In all the cases, the centers of the semicircular arcs lie below the real X-axis representing the non-Debye type dielectric relaxation behavior of the samples.[65] The two semicircular arcs corresponding to grain and grain boundary have been obtained from the recoded impedance spectra by Z-view software. The best fitting of the spectra was obtained using the electrical equivalent circuit consisting of resistance (R) and constant phase element (CPE). The capacitance values were calculated using the relationship, $C = (R^{1-n}C_Q)^{1/n}$, where the parameters C_Q and n are used to define CPE.[66] The resistance and capacitance values corresponding to the each contribution are provided in Fig. 8. The relaxation frequencies for grain and grain boundaries are obtained from the peak top of the complex plane plots by

using the relationship $\omega\tau_r$ (= $2\pi f_r RC$) = 1.[65] The increased values of real ($Z^{/}$) and imaginary ($Z^{//}$) part of complex impedance with decrease in temperature is associated with the decrease in the ac conductivity of the sample.[67] For pure NKN, the resistances of grains and grain boundaries at the temperatures of 300, 400 and 500^0C have been plotted with the inverse of temperature. The values of activation energies, calculated from the linear fit in the log (R_G, R_{GB}) vs 1000/T plot [Fig. 8 (g)], for grain [$E_{a(G)}$] and grain boundary [$E_{a(GB)}$] are 1.12 and 1.23 eV, respectively. These values of activation energies are associated with the movement of uncharged and charged oxygen vacancies.[68]

It is known that the simultaneous study of complex impedance (Z*) and complex modulus (M*) provides the entire spectrum of conduction mechanism, i.e., long range (from Z*) as well as localized conduction (from M*) occurring in the dielectric materials.[65,69] The values of real and imaginary components of electric modulus (M) have been calculated using the relationship, $M^{/}$= $2\ \pi f C_0\ Z^{//}$, $M^{//} = 2\ \pi f C_0\ Z^{/}$; where, f are C_0 are the frequency and open cell capacitance, respectively.[69] Fig. 9 shows the impedance and modulus spectroscopic plots for HA (Figs. 9. a, b), NKN (Figs. 9. c, d) and HA-NKN-HA (Figs. 9. e, f) at the temperatures of 500 and 400^0C, respectively. In case of pure HA and NKN, the spectroscopic plots reveal the relaxation peaks at temperatures above 200 and 300^0C, respectively. However, in case of HA-NKN-HA, the peaks in the spectroscopic plots are obtained at all the measuring temperatures upto 500^0C (figure not shown) probably because of the higher conductivity (space charge) of the sample due to the multilayered configuration. The maxima of impedance and modulus spectroscopic plots are positioned at different points on the frequency scale, representing the involvement of number of relaxation processes or non-Debye type behavior in the samples.[65] Also, the full width at half maxima (FWHM) is found to be more than 1.14 decades in frequency in the impedance

spectroscopic plots for HA, NKN and HA-NKN-HA samples, which are broader than the ideal Debye peak.[65] It suggests that the two different relaxation processes with comparative time constants overlap each other.[65] However, the modulus spectroscopic plot in pure HA at 500 and 400^0C show the Debye-type behavior, where the FWHM are 1.04 and 1.07, respectively in the measured range of temperature and frequency. The spectroscopic plots revealed almost symmetric peaks in case of pure HA and NKN, however, these peaks are asymmetric for HA-NKN-HA sample. The impedance spectroscopic plots for HA-NKN-HA appear to have the combination of two different peaks, because of the contribution from two phases/compositions with different conductivities. Hodge et al.[65] suggested that the separation between two peaks depend upon the conductivities of the different phases in the layered dielectrics.

The ratios of the peak heights of the impedance spectroscopic plots as the temperature is lowered from 500^0C to 400^0C for HA, NKN, HA-NKN-HA are about $6x10^2$, 15 and 15, respectively. This confirms the results obtained from complex plane plots that the resistance of the bulk/grain boundary increases with decrease in temperature, which indicates the presence of negative temperature coefficient of resistance.[65,69] The capacitance of a particular contribution is inversely proportional to the peak height of the modulus spectroscopic plot.[65] The differences in the peak heights suggest the variation of the capacitance with temperature. The decreased peak height (for pure HA and NKN) suggests the increased capacitance as the temperature is lowered from 500 to 400^0C. In the spectroscopic plots, the peak shifts towards the lower frequency side with decrease in the temperature which is characterized by the higher relaxation times. The variations in the peak position and height with temperature suggest that the dominant conduction mechanism is probably the hoping of charge carriers due to the thermal stimulation. Also, from the position of the peaks on the frequency scale, it can be inferred that the space charge and dipolar polarization

mechanisms are responsible for the observed phenomenon. The high sintering temperature creates the oxygen vacancies and other defects as discussed above in NKN and HA. The mobility of space charge, associated with the defects created due to the oxygen vacancies, increases with increase in temperature.[67] It has been suggested as the possible reason for the shift of relaxation peaks to the higher frequency side in the spectroscopic plots.[67]

The impedance spectroscopic analysis of the pig bone has been performed by Ciuchi et al.7 which demonstrated the piezoelectric behavior of bone as well. A very high impedance values were recorded for mechanically pressed bone as compared to that of the normal condition. Irrespective of anisotropic properties and pores, two semicircular arcs were observed in the mechanically pressed bone as compared to it's regular counterpart (one arc) which was suggested to occur due to the intrinsic origin of electrical response of mechanical stimulation.7

As a closure, Table 1 summarizes the physical, dielectric and electrical properties of the developed functionally graded HA-NKN-HA sample, which reveals the significant electrical activities in reference to the electrical properties of the natural bone.

3.6 *In vitro* cytocompatibility:

The *in vitro* cycompatibility assessment of developed compositions was performed using human osteoblast-like SaOS2 cells. As the initial cell adhesion has an important role in the subsequent cellular functionality such as proliferation,[70] the cells were cultured on the samples for 6 hrs to observe the initial adhesion as well as the morphology of cells. Okumura et al.[70] demonstrated that the initial adhesion of SaOS2 cells depends on the substrate and such report on NKN phase is scars in the literatures. Therefore, the initial adhesion test was performed. The fluorescence microscopy observation (Fig. 10) reveals that the cells are adhered and flattened well with their spreaded cytosketon on all the developed sample surfaces. The NKN shows the similar morphology as that of pure HA. The proliferation behavior of SaOS2 cells was studied after 1, 3

and 5 days of incubation, respectively. Fig. 11 demonstrate the time dependent proliferation behavior of SaOS-2 cells on HA, HA-NKN-HA and NKN samples. The statistically significant ($p < 0.05$) increase in the cell proliferation with increase in the culture duration is observed on the examined sample surfaces. Interestingly, NKN exhibits the higher rate of proliferation as compared to the other samples for culture duration of up to 5 days. In addition to the surface chemistry, the polarizability and AC conductivity of NKN are significantly higher than that of pure HA. Greeshma et al.[71] demonstrated that the cell growth and proliferation is the function of conductivity of biomaterial substrate. The higher polarizability and conductivity of NKN can be one of the possible reasons for better cell proliferation performance as compared to the other samples.

It needs to be mention here that in our earlier report,[72] we have demonstrated that the space charge polarization of lithium-modified sodium potassium niobate has increased the *in vitro* bioactivity. Therefore, the present study togetherwith the earlier results can conclusively suggest that the NKN can be potential alternative for hard tissue replacement applications.

4. Conclusions

The present study reveals that the electrical polarizability of hydroxyapatite can be enhanced significantly to realize the bone-like electrical properties, using the biocompatible sodium potassium niobate piezoelectrics as an intermediary layer. The delamination of the layers or the crack formation has been avoided by inserting the buffer interlayers between HA and NKN layers and adopting the optimal spark plasma sintering conditions. The developed functionally graded bioelectroceramics can be used to achieve the desired combination of electrical and mechanical properties without affecting the bioactivity of hydroxyapatite. From the measurement of activation energy and the available literature report, it can be suggested that the proton

conduction is the dominant conduction mechanism in HA and HA-NKN-HA samples, whereas the movement of oxygen vacancies are responsible for conduction in NKN.

In addition to the enhanced polarizability of hydroxyapatite, this study also demonstrated good *in vitro* cytocompatibility of sodium potassium niobate ceramics. Such functionally graded biceramics can be a potential electroactive orthopedic implant material.

5. Acknowledgements

The present work is supported by Grant-in-Aids for JSPS Challenging Exploratory Research (No.2365400) and for JSPS Fellows (No.24-2377). AKD gratefully acknowledge JSPS for the fellowship.

References

[1] E. Fukada and I.Yasuda. *J. Phys. Soc. Jap.*, 1957, **12**, 1158.

[2] C.J. Dreyer. *Nature*, 1961, **90**, 1217.

[3] S.B. Lang. *Nature*, 1966, **212**, 704.

[4] A. Salleo. *Life Scipt.* 1967, **2**, 2651.

[5] M.A. EI Messiery, G.W. Hastings, S. Rakawski. *J. Biomed. Eng.*, 1979, **1**, 63.

[6] A. A. Marino and R. O. Becker. *Nature*, 1970, **228**, 473.

[7] I. V. Ciuchi, L. P. Curecheriu, C. E. Ciomaga, A. V. Sandu and L. Mitoseriu. J. Adv. Res. Phys., 2010, **1(1)**, 011007.

[8] F.R. Baxter, C.R. Bowen, I.G. Turner, A.C.E. Dent. *Ann. Biomed. Eng.*, 2010, **38(6)**, 2079.

[9] G.W. Hastings and F.A. Mahmud. *J. Biomed. Eng.* 1988, 10, 515.

[10] B. M. Isaacson and R. D. Bloebaum. *J. Biomed. Mater. Res. Part A*., 2010, **95A**, 1270.

[11] S. Mascarenhas. *Ann. N. Y. Acad. Sci.*, 1974, **238**, 36-52.

[12] R. Knoppers, J. W. Gunnink, J. Van den Hout and W. Van Vliet., *TNO Science and Industry, The Netherlands*, 2004, SFF2004, pp 38-43.

[13] R. M. Mahamood, E. T. Akinlabi, M. Shukla and S. Pityana. *Proceedings of WCE*, 2012, 3, July 4 - 6, 2012, London, U.K.

[14] W. Pompea, H. Worch, M. Epple, W. Friess, M. Gelinsky, P. Greil, U. Hempele, D. Scharnweber and K. Schulte. *Mat. Sci. Eng. A*, 2003, **362**, 40.

[15] N. C. Teng, S. Nakamura, Y. Takagi, Y. Yamashita, M. Ohgaki and K. Yamashita. *J. Dent. Res.*, 2001, **80**, 1925.

[16] J. Q. Feng, H. P. Yuan and X. D. Zhang. *Biomater.*, 1997, **18**, 1531.

[17] S.A.W. Pickering and B.E. Scammell. *Low. Extremity Wounds*, 2002, **1(3)**, 152.

[18] J.T. Ryaby. *Clin. Orthop.*, 1998, **355**, S205.

[19] M. Oishi, S.T. Onesti. *Neurosurgery*, 2000, **47**, 1041.

[20] D. Kumar, J.P. Gittings, I.G. Turner, C.R. Bowen, L.A. Hidalgo-Bastida and S.H. Cartmell. Acta Biomater., 2010, **6(4)**,1549.

[21] A. K. Dubey, S. D. Gupta and B. Basu. *J. Biomed. Mater. Res.- B*, 2011, **98 B**, 18.

[22] A. K. Dubey, P. Agrawal, R.D.K. Misra and B. Basu. *J. Mater. Sci. Mater. Med.*, 2013, **24**, 1789.

[23] A. K. Dubey and B. Basu. *J. Am. Ceram. Soc.*, 2014, **97(2)**, 481.

[24] M. H. Fathi, V. Mortazavi, S. I. R. Esfahani. *Dent. Res. J.*, 2008; **5(2)**:81-87.

[25] A. Sobczak, Z. Kowalski and Z. Wzorek. *Acta Bioeng. Biomech.*, 2009, **11 (4)**, 23.

[26] K. Kakimoto, Y. Hayakawa and I. Kagomiya. *J. Am. Ceram. Soc.*, 2010, **93**, 2423.

[27] K. Nilsson, J. Lidman, K. Ljungstrom, C. Kjellman, Biocompatible material for implans, U.S. patent 6,526,984 B1, 2003.

[28] Q. Wang, J. Yang, W. Zhang, R. Khoie, Y. Li, J. Zhu and Z. Chen. *Int. J. Oral Sci.*, 2009, **1(2)**, 99.

[29] A. Jalalian and A. M. Grishin. *Appl. Phys. Lett.*, 2012, **100**, 012904.

[30] R. Olivares-Navarrete, J. J. Olaya, C. Ramirez, S. E. Rodil. Coatings, 2011, **1**, 72.

[31] S. Reddy, A. K. Dubey, B. Basu, R. Guo and A.S. Bhalla. Int. Ferroelect., 2011, **131(1)**, 147.

[32] K. Shibata, K. Suenaga, A. Nomoto, and T. Mishima, *Jpn. J. Appl. Phys.*, 2009, **48**, 121408.

[33] Y. Guo, K. Kakimoto and H. Ohsato, *Appl. Phys. Lett.*, 2004, **85 (18)**, 4121.

[34] K. Kobayashi, Y. Doshida, Y. Mizuno and C. A. Randall. *J. Am. Ceram. Soc.*, 2012, **95 (9)**, 2928.

[35] J. Abe, M. Kobune, K. Kitada, T. Yazawa, H. Masumoto and T. Goto. *J. Korean Phys. Soc.*, 2007, **51 (2)**, 810.

[36] J.P. Gittings, C.R. Bowen, A.C.E. Dent, I.G. Turner, F.R. Baxter and J.B. Chaudhuri. Acta Biomater., 2009, **5(2)**, 743.

[37] V.P. Orlovskii, N.A. Zakharov, A.A. Ivanov. *Inorg. Mater*., 1996, **32(6)**, 654.

[38] J.P. Gittings, C.R. Bowen, I.G. Turner, F. Baxter, J. Chaudhuri. *J. Eur. Ceram. Soc.*, 2007, **27**, 4187.

[39] B. Harihara, B. Venkataraman and K. B. R. Varma. *Solid State Ionics*, 2004, **167**, 197.

[40] D. P. Almond, C. R. Bowen and D. A. S. Rees. *J. Phys. D: Appl. Phys.*, 2006, **39**, 1295.

[41] E. Marzec. Bioelectroch. Bioener. 1998, **46**, 29.

[42] D. Miklavcic, N. Pavselj and F. X. Hart, Electric Properties of Tissues. Wiley Encyclopedia of Biomedical Engineering, 1-12, 2006.

[43] C. Gabriel, S. Gabriel and E. Corthout. *Phys. Med. Biol.*, 1996, **41**, 2231.

[44] M. Fois, A. Lamure, M. J. Fauran and C. Lacabanne. Dielectric Properties of Bone and its Main Mineral Component, 10th International Symposium on Electrets, *IEEE*, 217-220, 1999.

[45] M.H. Shames and L.S. Lavine. *Clin. Orthop.*, 1964, **355**, 177.

[46] P. A. Williams and S. Saha. Ann. Biomed. Eng., 1996, **24**, 222.

[47] M.P. Mahabole, R.C. Aiyer, C.V. Ramakrishna, B. Sreedhar, R.S. Khairnar. Bull. Mater. Sci., 2005, **28**, 535.

[48] H. Den Hartog, D. O. Welch, B.S.H. Royce. *Phys. Stat. Sol. (B)*, 1972, **53(1)**, 201.

[49] N. A. Zakharov, *Tech. Phys. Lett.*, 2001, **27(12)**, 1035.

[50] N. Horiuchi, M. Nakamura, A. Nagai, K. Katayama and K. Yamashita. *J. Appl. Phys.* 2012, **112**, 074901.

[51] N. A. Zakharov and V. P. Orlovskii. *Tech. Phys. Lett.,* 2001, **27(8)**, 629.

[52] V. P. Orlovskii, N. A. Zakharov, A. A. Ivanov. *Inorg. Mater.*, 1996, **32(6)**, 654.

[53] N. Horiuchi, J. Endo, N. Wada, K. Nozaki, M. Nakamura, A. Nagai, K. Katayama and K. Yamashita, *J. Appl. Phys.*, 2013, **113**, 134905.

[54] N.A. Zakharov, V.P. Orlovskii. *Tech. Phys. Lett.*, 2001, 27(8), 629.

[55] G. C. Maiti and F. Freund. *J. Chem. Soc. Dalton Trans.*, 1981, 6, 949.

[56] A.K. Jonscher. *Nature*, 1977, **267**, 673.

[57] G. B. Reinish and A. S. Nowick. J. Electrochem. Soc., 1976, **123**, 1451.

[58] T. Kijima and M. Tsutsumi, *J. Am. Ceram. Soc.*, 1979, **62**, 455.

[59] K. Yamashita, K. Kitagaki and T. Umegaki. *J. Am. Ceram. Soc.*, 1995, **78**, 1191.

[60] A. Laghzizil, N. El Herch, A. Bouhaouss, G. Lorente and J. Macquete. *J. Solid State Chem.,* 2001, **156**, 57.

[61] A. Laghzizil, N. Elherch, A. Bouhaouss, G. Lorente, T. Coradin, J. Livage. *Mater. Res. Bull.* 2001, **36**, 953.

[62] N. Yamazoe and Y. Shimizu. *Sensor. Actuator.*, 1986, **10**, 379.

[63] M. Nagai and T. Nishino. *Solid State Ionics*, 1988, **28**, 1456.

[64] G.W. Hastings, M. A. ElMessiery and S. Rakowski. *Biomater.*, 1981, **2**, 225.

[65] I. M. Hodge, M. D. Ingram and A. R. West. *J. Electroanal. Chem.*, 1976, **74**, 125.

[66] X. Guo, W. Sigle and J. Maier. *J. Am. Ceram. Soc.*, 2003, **86 (1)**, 77.

[67] E. M. Alkoy and A. Berksoy-Yavuz. *IEEE Trans. Ultrason. Ferroelectr. Freq. Control.*, 2012, **59(10)**, 2121.

[68] C. H. Park. *J. Korean Phys. Soc.*, 2003, **42**, S1420.

[69] R. Rani, S. Sharma, R. Rai and A. L. Kholkin. *J. Appl. Phys.*, 2011, **110**, 104102.

[70] A. Okumura, M. Goto, T. Goto, M. Yoshinari, S. Masuko, T. Katsuki and T.Tanaka, *Biomater.*, 2001, **22**, 2263.

[71] G. Thrivikraman, P. K. Mallik and B. Basu. *Biomater.*, 2013, **34**, 7073.

[72] A. K. Dubey, H. Yamada and K. Kakimoto. *J. Appl. Phys.*, 2013, **114**, 124701.

Legends

List of Tables:

Table 1: Summary of the physical, dielectric and electrical properties of the developed functionally graded HA-NKN-HA sample

List of Figures:

Fig. 1: (a) The spatial distribution of HA, buffer and NKN layers in the developed functionally graded material (HA-NKN-HA) and (b) sintering cycle adapted to process the samples.

Fig. 2: X-ray diffraction spectra for HA, NKN and FGM HA-NKN-HA.

Fig. 3: SEM micrographs revealing the morphology of fractured surfaces of the developed functionally graded HA-NKN-HA sample acquired from (a, c) the interface region between HA and buffer layers and (b, d) the interface region between buffer and NKN layers.

Fig. 4: Temperature dependent dielectric constant and loss spectra at few fixed frequencies (a, c and e), frequency dependent dielectric constant spectra at few isothermal temperatures (b, d and f).

Fig. 5: Variation of AC conductivity with temperature for (a) HA, (b) NKN and (c) HA-NKN-HA. (d) represents the dependence of AC conductivity on temperature at the crossover frequencies for HA and HA-NKN-HA.

Fig. 6: Variation of phase angle with frequency at a few selected temperatures for (a) HA, (b) NKN, (c) HA-NKN-HA compositions and (d) shows the electromechanical coupling coefficient computation using impedance and phase angle spectra.

Fig. 7: P-E hysteresis loop for the developed FGM HA-NKN-HA

Fig. 8: Complex plane impedance plots for HA (a, b), NKN (c, d) and HA-NKN-HA (e, f) compositions at 500 and 400^0C. The insets illustrate the electrical equivalent circuit, containing

the values of the resistances and constant phase elements, used to obtain the best fit results from Z-view software. The corresponding values of the capacitances are also shown in brackets.

Fig. 9: Impedance and modulus spectroscopic plots for HA (a, b), NKN (c, d) and HA-NKN-HA (e, f) compositions at 500 and 400^0C.

Fig. 10: The fluorescence microscopic images revealing the morphology of human osteoblast-like SaOS2 cells, while cultured on (a) HA, (b) HA-NKN-HA and (c) NKN for 6 hrs. The micron bars correspond to 50 μm.

Fig. 11: The proliferation behavior of human osteoblast-like SaOS2 cells, cultured on HA, HA-NKN-HA and NKN for 1, 3 and 5 days, respectively. The asterisk marks (*) and (**) represent the statistically significant increase in the cell proliferation after 3 and 5 days of culture, respectively with reference to the cells cultured for 1 day on the same sample ($p < 0.05$).

Table 1: Summary of the physical, dielectric and electrical properties of the developed functionally graded HA-NKN-HA sample

Material	ρ (gm/cm^3)	ε_r (@ 10 kHz)	σ_{ac} $(ohm\text{-}cm)^{-1}$ (@ 10 kHz)	E_a (eV)	ρ_{dc} (ohm-cm)	d_{33} (pC/N)	k_p	Q_m	E_c (kV/cm)	P_r ($\mu C/cm^2$)
HA-NKN-HA	3.93	38	5.7×10^{-9}	0.69	2.0×10^{13}	4.2	0.17	81	0.76	0.06

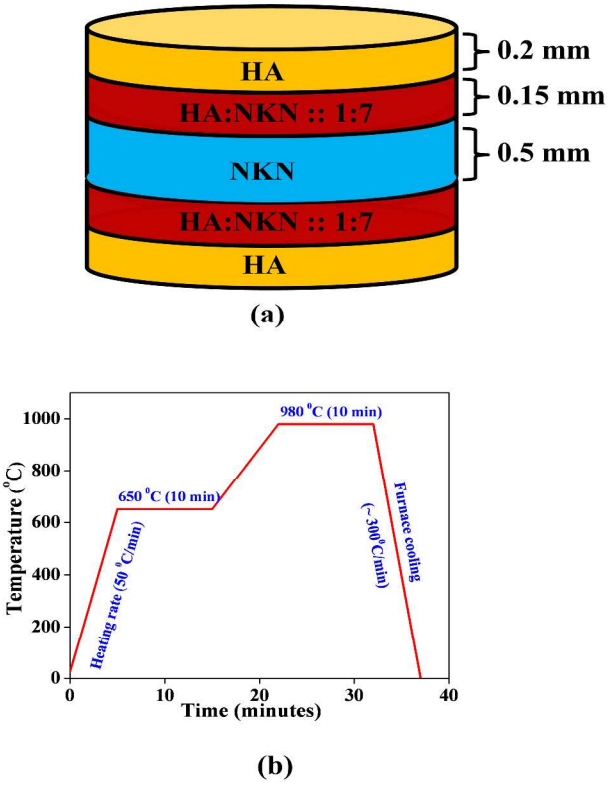

Fig. 1: (a) The spatial distribution of HA, buffer and NKN layers in the developed functionally graded material (HA-NKN-HA) and (b) sintering cycle adapted to process the samples.

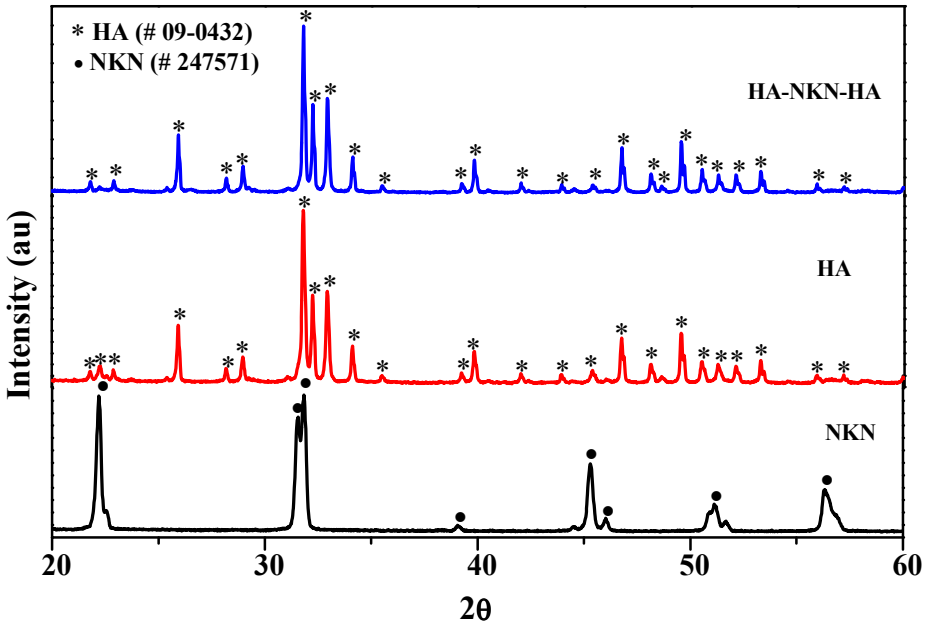

Fig. 2: X-ray diffraction spectra for HA, NKN and FGM HA-NKN-HA.

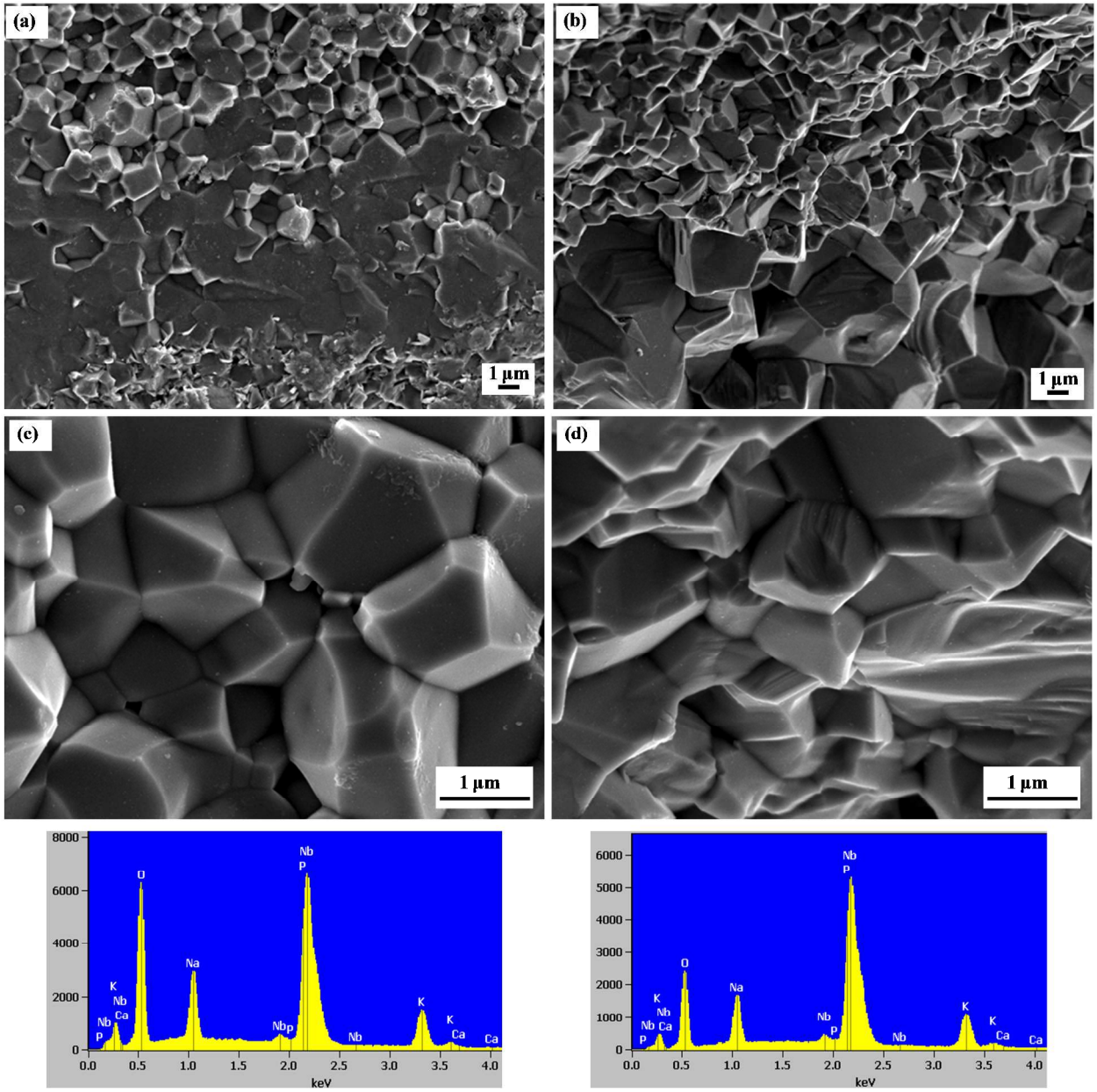

Fig. 3: SEM micrographs revealing the morphology of fractured surfaces of the developed functionally graded HA-NKN-HA sample acquired from (a, c) the interface region between HA and buffer layers and (b, d) the interface region between buffer and NKN layers.

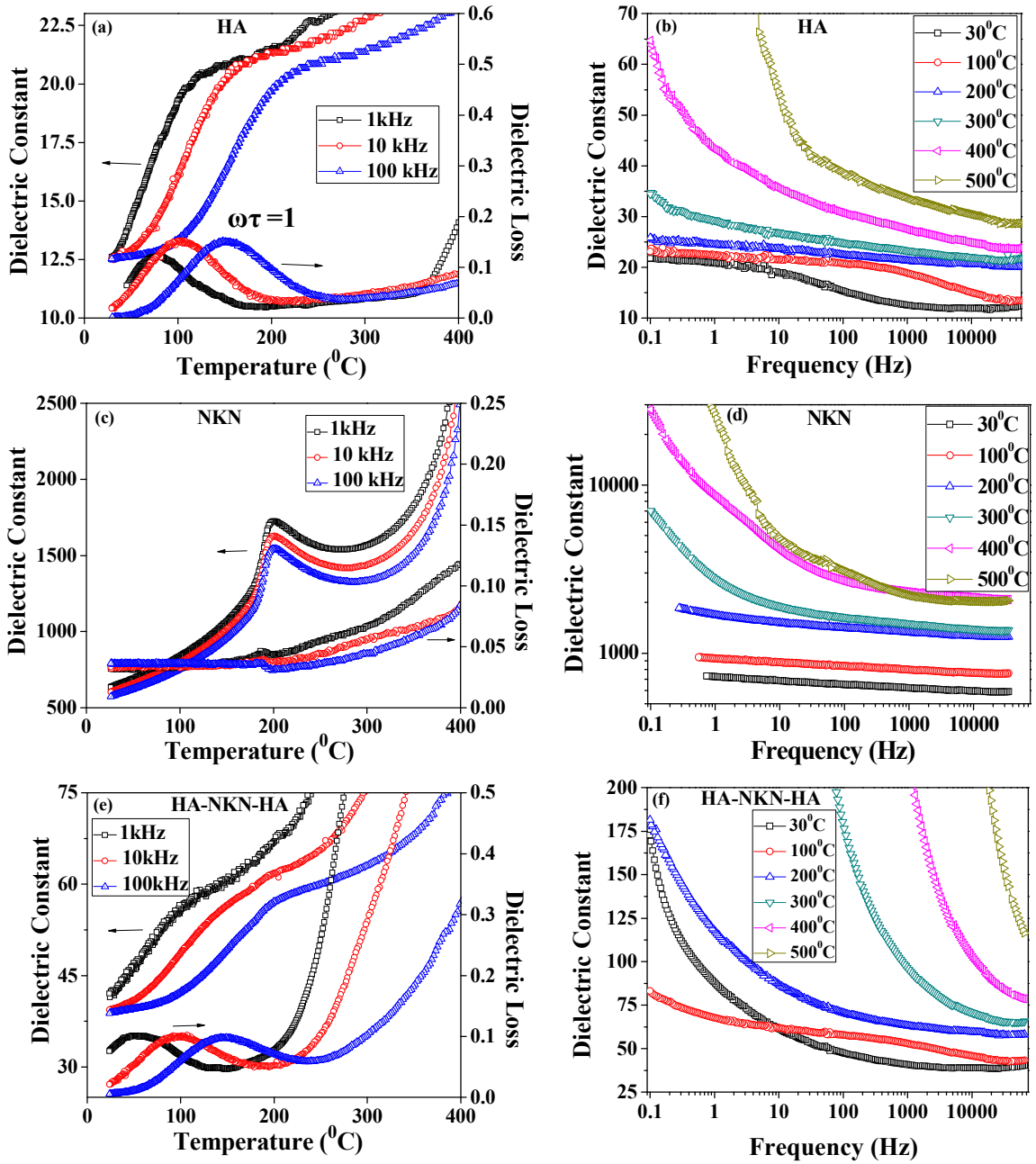

Fig. 4: Temperature dependent dielectric constant and loss spectra at few fixed frequencies (a, c and e), frequency dependent dielectric constant spectra at few isothermal temperatures (b, d and f).

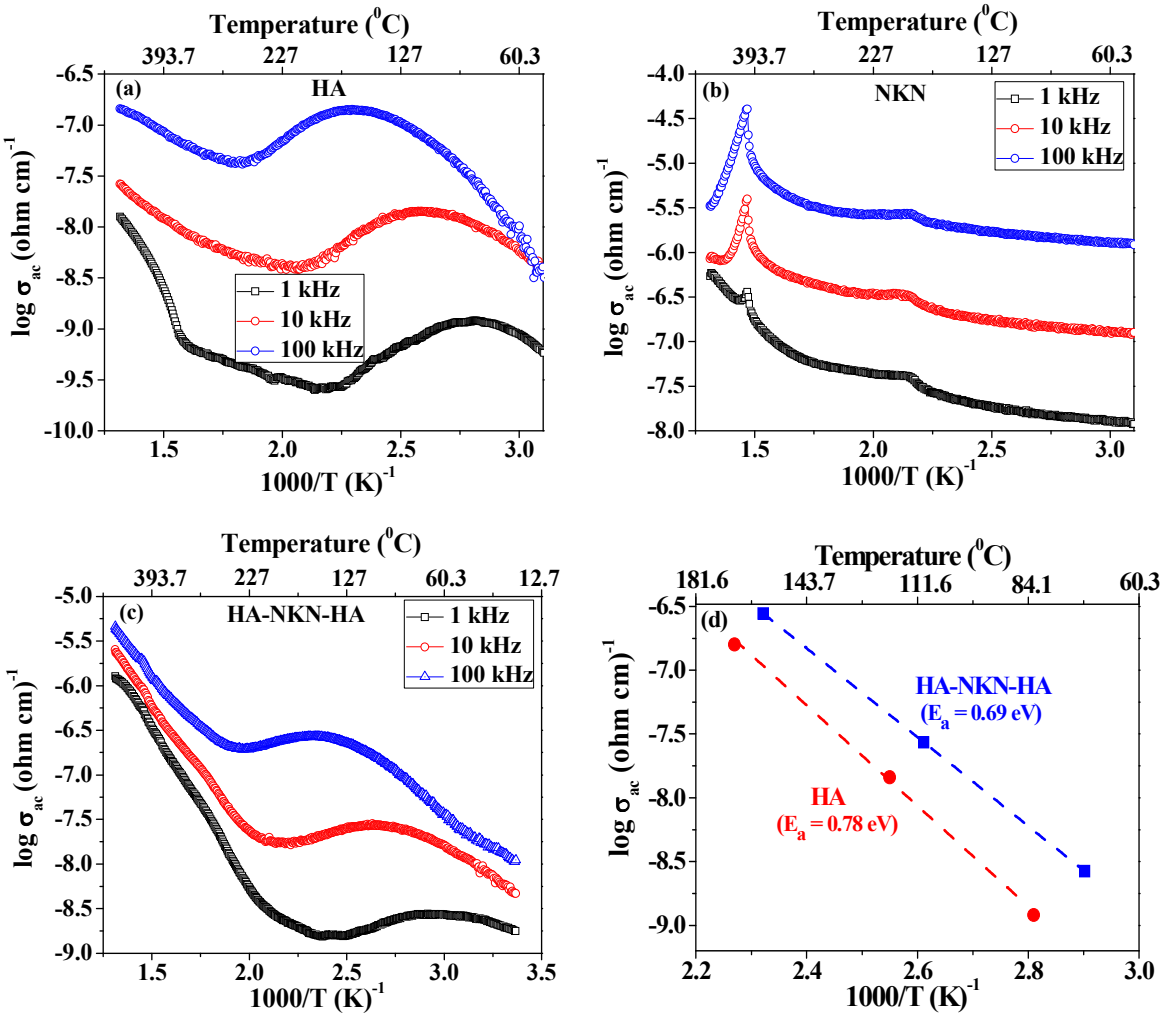

Fig. 5: Variation of AC conductivity with temperature for (a) HA, (b) NKN and (c) HA-NKN-HA. (d) represents the dependence of AC conductivity on temperature at the crossover frequencies for HA and HA-NKN-HA.

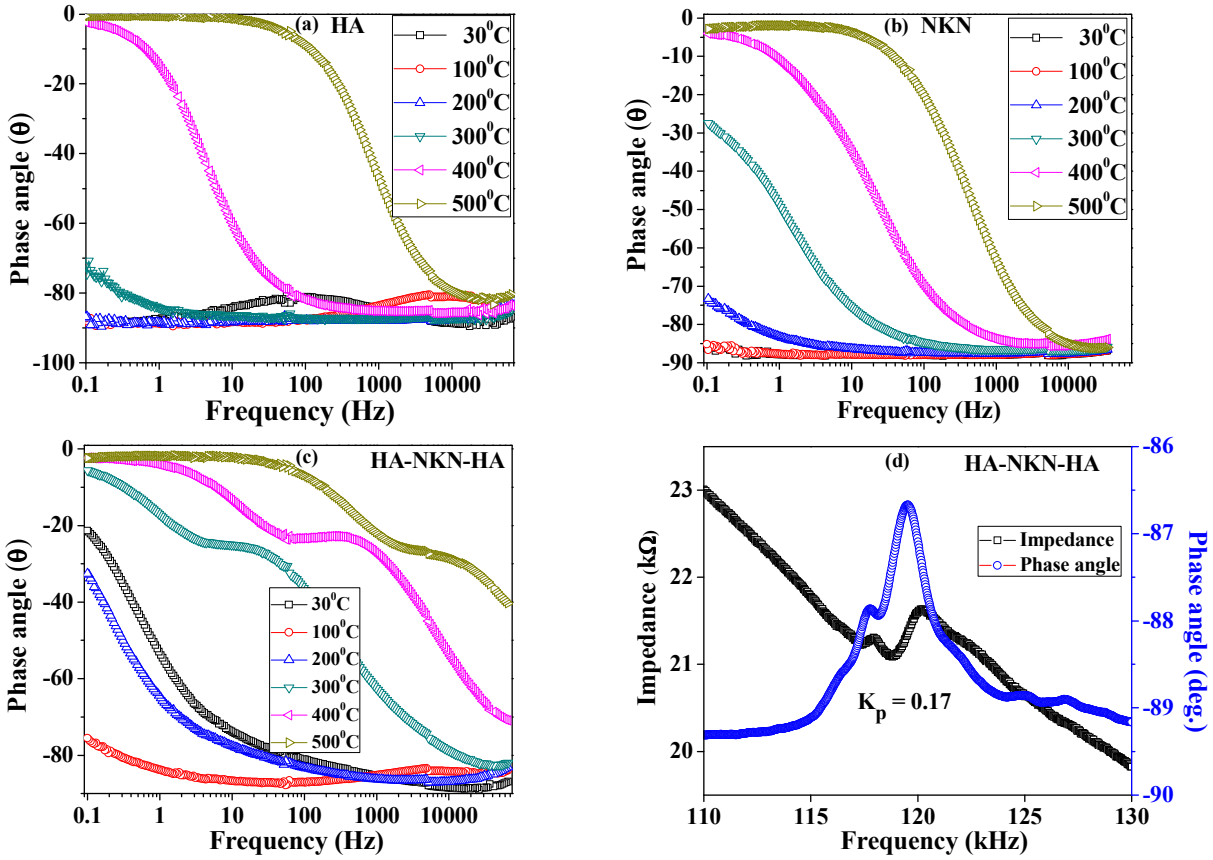

Fig. 6: Variation of phase angle with frequency at a few selected temperatures for (a) HA, (b) NKN, (c) HA-NKN-HA compositions and (d) shows the electromechanical coupling coefficient computation using impedance and phase angle spectra.

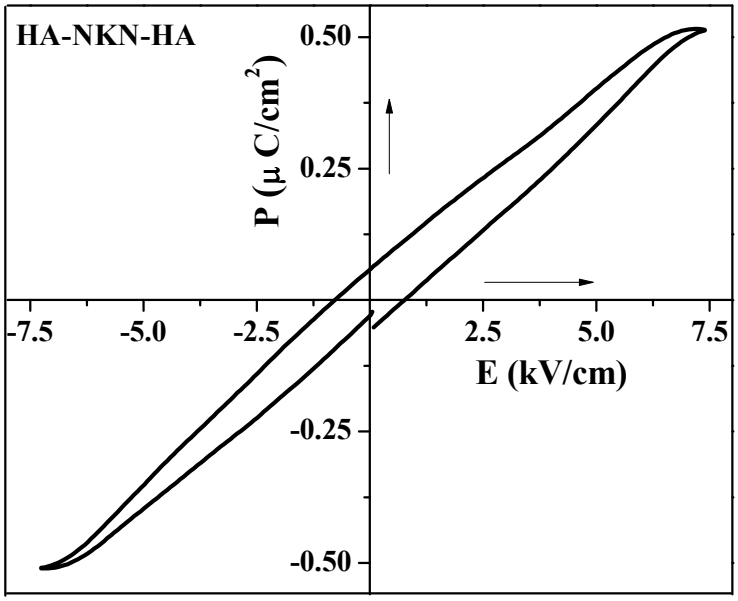

Fig. 7: P-E hysteresis loop for the developed FGM HA-NKN-HA

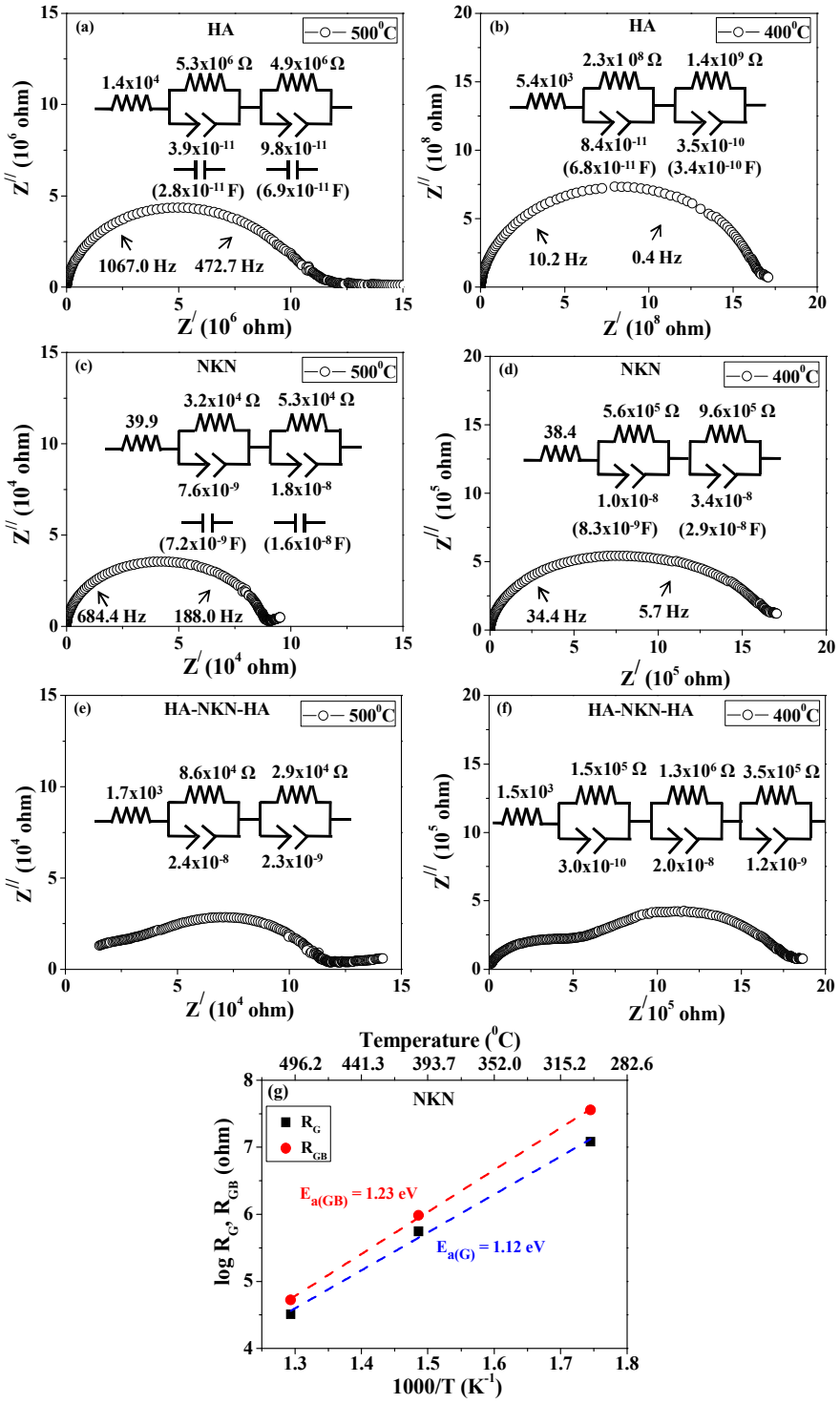

Fig. 8: Complex plane impedance plots for HA (a, b), NKN (c, d) and HA-NKN-HA (e, f) compositions at 500 and 400^{0}C. The insets illustrate the electrical equivalent circuit, containing the values of the resistances and constant phase elements, used to obtain the best fit results from Z-view software. The corresponding values of the capacitances are also shown in brackets.

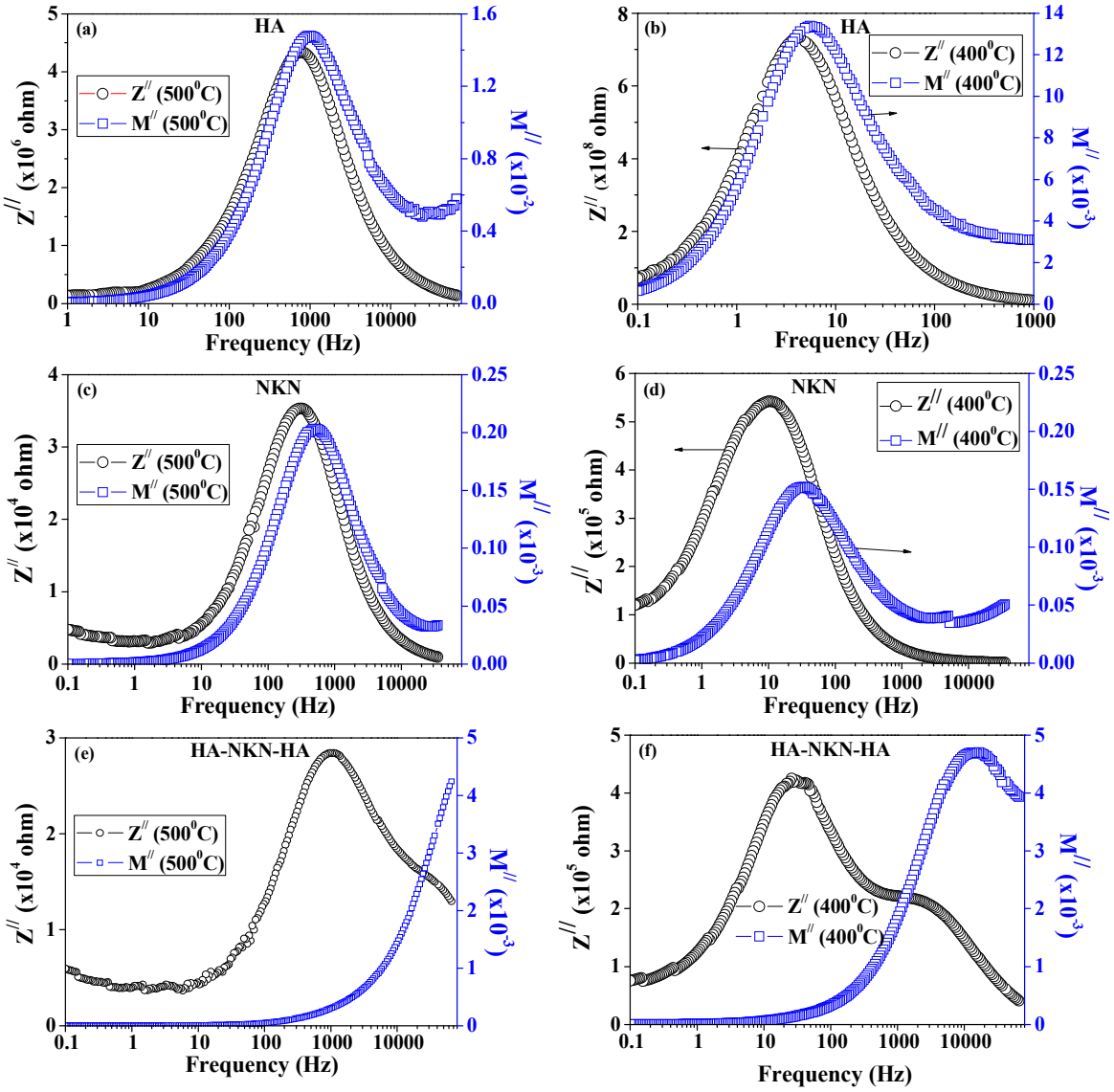

Fig. 9: Impedance and modulus spectroscopic plots for HA (a, b), NKN (c, d) and HA-NKN-HA (e, f) compositions at 500 and 400^{0}C.

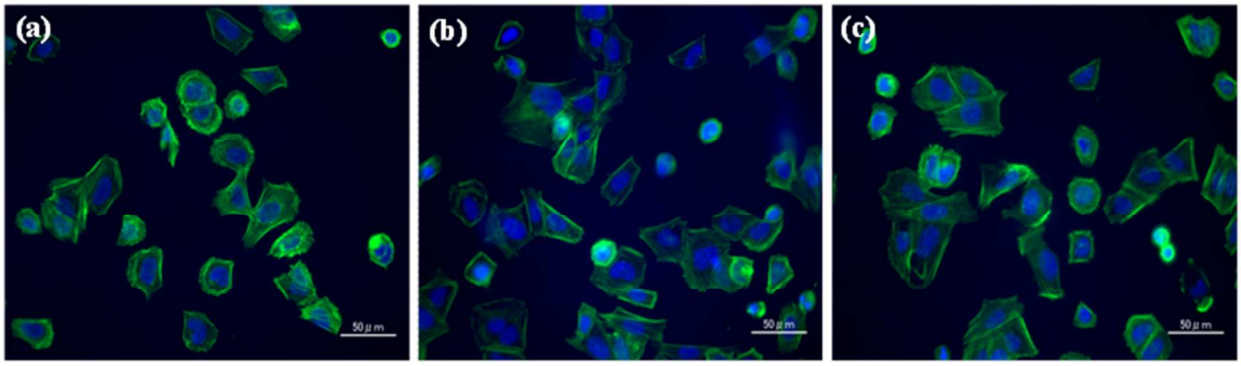

Fig. 10: The fluorescence microscopic images revealing the morphology of human osteoblast-like SaOS2 cells, while cultured on (a) HA, (b) HA-NKN-HA and (c) NKN for 6 hrs. The micron bars correspond to 50 μm.

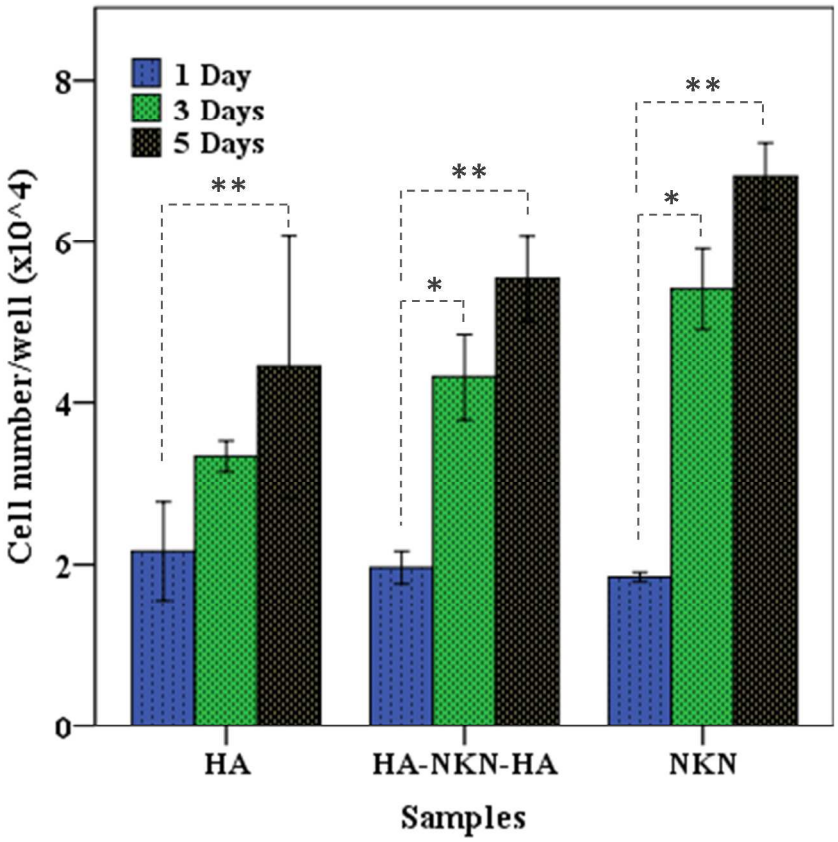

Fig. 11: The proliferation behavior of human osteoblast-like SaOS2 cells, cultured on HA, HA-NKN-HA and NKN for 1, 3 and 5 days, respectively. The asterisk marks (*) and (**) represent the statistically significant increase in the cell proliferation after 3 and 5 days of culture, respectively with reference to the cells cultured for 1 day on the same sample ($p < 0.05$).